Research Square

Preprints are preliminary reports that have not undergone peer review.
They should not be considered conclusive, used to inform clinical practice,
or referenced by the media as validated information.

Structural, Morphological and Optical Properties of Cd0.7Fe2.3O4 Thin Films Deposited on Glass and Quartz Substrates and Electrical Investigation of Cd0.7Fe2.3O4/n-Si heterostructure.

M. Smiti
University of Gabes
S. Mourad
University of Gabes
Rehab Ramadan Shehata Ali
Minia University
R. J. Martín-Palma
Universidad Autónoma de Madrid
Ahmed Slimani
Sorbonne University Abu Dhabi, Al Reem Island
O. Amorri
University of Gabes
F. Tiss
University of Gabes
Kamel Khirouni
Kamel.Khirouni@fsg.rnu.tn
University of Gabes
E. Dhahri
University of Sfax

Research Article

Keywords: Thin films of ferrite, spray pyrolysis, structural and optical properties, current-voltage characteristic (I(V)).

Posted Date: June 4th, 2026

DOI: https://doi.org/10.21203/rs.3.rs-9681319/v1

License: This work is licensed under a Creative Commons Attribution 4.0 International License.
Read Full License

Additional Declarations: No competing interests reported.

Version of Record: A version of this preprint was published at Journal of Materials Science: Materials in Electronics on October 17th, 2026. See the published version at https://doi.org/10.1007/s10854-026-18638-2.

Structural, Morphological and Optical Properties of $Cd_{0.7}Fe_{2.3}O_4$ Thin Films Deposited on Glass and Quartz Substrates and Electrical Investigation of $Cd_{0.7}Fe_{2.3}O_4$/n-Si heterostructure.

M. Smiti[1], S. Mourad[1], Rehab Ramadan Shehata Ali[2], R.J. Martín-Palma[3], Ahmed Slimani[4], O. Amorri[1], F. Tiss[1], K. Khirouni[1*], E. Dhahri[5].

[1] Laboratory of Physics of Materials and Nanomaterials Applied to the Environment, Faculty of Sciences of Gabes, University of Gabes, 6079 Gabes, Tunisia.

[2] Department of Physics, Faculty of Science, Minia University, Minia 61519, Egypt

[3] Departamento de Física Aplicada and Instituto Universitario de Ciencia de Materiales "Nicol´as Cabrera" (INC), Universidad Autónoma de Madrid, Campus de Cantoblanco, 28049 Madrid, Spain

[4]Sciences and Engineering Department, Sorbonne University Abu Dhabi, Al Reem Island, P.O. Box 38044, Abu Dhabi, UAE

[5] Laboratory of Applied Physics, Faculty of Sciences, University of Sfax, Tunisia.

[*]Corresponding author: Kamel Khirouni, Kamel.Khirouni@fsg.rnu.tn/

Abstract

Thin films of $Cd_{0.7}Fe_{2.3}O_4$ were deposited by spray pyrolysis on glass, quartz, and n-type silicon substrates, and the effect of annealing temperature on their structural, optical, and electrical properties was investigated. XRD results confirm the formation of a spinel structure after annealing, accompanied by improved crystallinity. Optical measurements reveal strong absorption in the UV–visible range, with a band gap varying from 3.14 to 3.85 eV. FTIR analysis confirms the presence of Cd–O and Fe–O bonds. Electrical characterization of the $Cd_{0.7}Fe_{2.3}O_4$/n-Si heterostructure shows rectifying behavior, with the ideality factor decreasing from 6 to 1 as temperature increases, indicating improved carrier transport. These results demonstrate the potential of this material for electronic and optoelectronic applications.

Keywords:

Thin films of ferrite, spray pyrolysis, structural and optical properties, current-voltage characteristic (I(V)).

1. Introduction

Spinel-type ferrites, widely recognized as magnetic materials, have been the subject of numerous studies. These studies have explored both their fundamental properties and their technological applications, particularly their magnetic, electrical, and optical behavior. The general formula for spinel ferrite is AFe_2O_4, where A (the tetrahedral site) is occupied by a divalent metal ion and B (the octahedral site) is occupied by a trivalent metal ion. Their growing interest stems from their tunable electrical resistivity and magnetic properties, particularly applications in high-frequency devices [1].

Among these materials, cadmium ferrite ($CdFe_2O_4$) has attracted considerable attention due to its superior electromagnetic properties, remarkable chemical stability, low coercivity, and moderate saturation magnetization. These characteristics make it suitable for applications such as soft magnets and low-loss materials at high frequencies [2]. It has been determined that $CdFe_2O_4$ has a cubic crystal structure [3].

Various techniques for synthesizing spinel ferrite nanoparticles are described in the literature. The most well-known techniques are solid-state reaction [4], the sol-gel process [5], and combustion synthesis [6]. While bulk spinel ferrites have been extensively studied, increasing attention has recently been devoted to their thin-film counterparts, due to the enhanced control over their structural and functional properties. Advanced fabrication methods such as atomic layer deposition [7], chemical vapor deposition (CVD) [8], and spray pyrolysis [9] have been employed to ensure precise control over morphology and composition.

Recent developments in metal-oxide semiconductor heterojunctions have attracted considerable interest, particularly due to their potential for next-generation electronic and optoelectronic devices. Cadmium ferrite, characterized by a relatively narrow band gap and high chemical stability, has emerged as a promising material for diode-related applications due to its exceptional magnetic and electrical properties. When integrated with silicon substrates, heterojunctions can exhibit rectifying behavior. This makes such structures suitable photodetectors, sensors, and solar energy conversion systems [10–14].

Traditional methods for analyzing diode characteristics, such as current-voltage (I-V) measurements, provide essential information about their electrical performance. In the present work, $Cd_{0.7}Fe_{2.3}O_4$ thin films were prepared using the spray pyrolysis method. The structural, morphological, and optical characteristics of the fabricated films were systematically analyzed. In addition, a $Cd_{0.7}Fe_{2.3}O_4$/n-Si heterostructure was fabricated, and its electrical characteristics were investigated. The I–V, C–V, and conductance–frequency (G–ω) characteristics were analyzed, to evaluate the suitability of this heterostructure for applications in electronics and optoelectronics.

2. Experimental details

2. 1. Synthesis

To use the spray pyrolysis technique, a stable, homogenous solution containing the chemical components must be obtained. Consequently, the right solvents and precursors need to be selected, Cadmium nitrate tetrahydrate ($Cd(NO_3)_2.4H_2O$) and iron (III) nitrate nonahydrate ($Fe(NO_3)_3.9H_2O$) were employed as starting materials. The amounts of the reactants are weighed using an electronic balance in accordance with the stoichiometric ratios of the chemical equation for the following reaction:

$$\mathbf{0.7\ Cd(NO_3)_2.4H_2O + 2.3\ Fe(NO_3)_3.9H_2O \longrightarrow Cd_{0.7}Fe_{2.3}O_4 + gaz\uparrow} \quad \mathbf{(1)}$$

The synthesis protocol is presented in **Fig. 1**. In fact, we dissolved 0.3g $Fe(NO_3)_3 9H_2O$ in 3 ml dimethyl formamide (DMF) in one beaker (A1) and 0.3 g $Cd(NO_3)_2.4H_2O$ in 2 ml DMF in another beaker (A2). The two solutions obtained were kept under magnetic stirring. After one hour, the two solutions were mixed. A quantity of 10 ml of ethylene glycol was introduced into the solution and kept under stirring until complete dissolution. Finally, the solution was diluted one more time with 10 ml ethylene glycol and left in the dark for 36 hours to check any precipitation. A multi-step procedure that included treatment with trichloroethylene, acetone, distilled water and ethanol for 15 min each was used to clean all substrates. The solution was then sprayed onto preheated glass, quartz and n-type silicon substrates. the values of optimal deposition parameters, including spray pressure and flow rate are regrouped in **table 1**. The

obtained layers were annealed at 600°C, 750 °C and 900 °C for 2h under ambient atmospheric. After deposition, both the front and back contacts were coated using the thermal evaporation process using silver to achieve ohmic contact. The structure is depicted in **Fig. 2**.

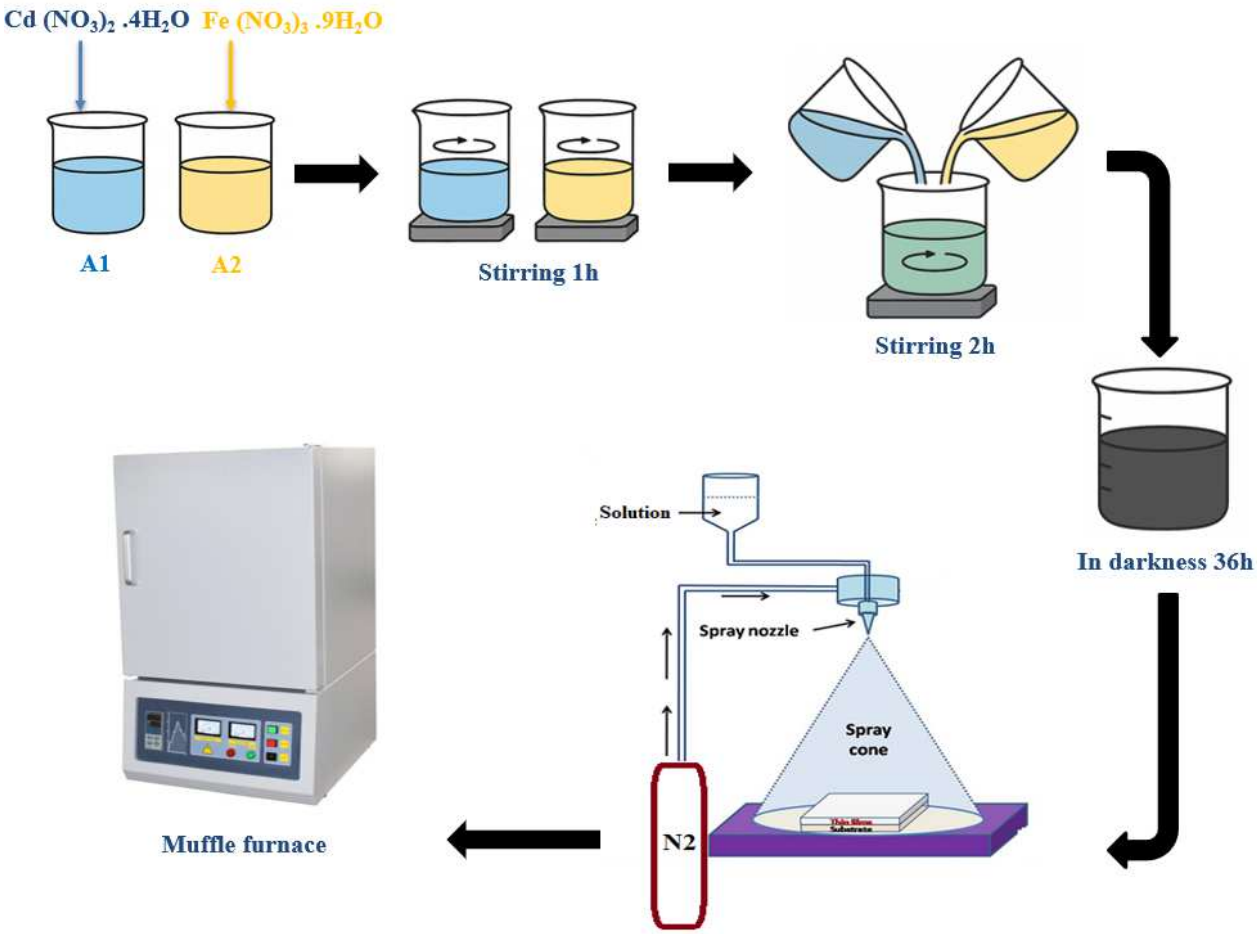


Fig. 1: Schematic representation of the $Cd_{0.7}Fe_{2.3}O_4$ thin films deposition process using spray pyrolysis method.

Table 1: Optimized parameters of spray deposition of thin films

	$Cd_{0.7}Fe_{2.3}O_4$
Solution flow rate	**0.5 ml/min**
Deposit time	**10 min**
Substrate temperature	**350 °C**
Volume of used solution	**7 ml**
Nitrogen pressure	**0.5 bar**

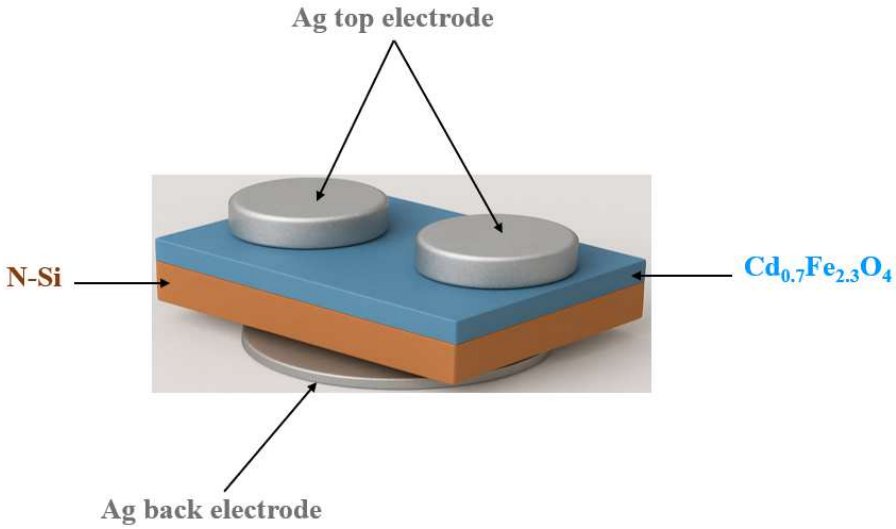


Fig. 2: The schematic of $Cd_{0.7}Fe_{2.3}O_4$/N-Si structure.

2. 2. Characterizations

A Panalytic X'pert PRO X-ray diffractometer with radiation wavelength $\lambda_{Cu\text{-}K\alpha}$ = 1.5418 Å was used for structural investigation within a 2θ range of 25° to 50°. Scanning electron microscopy (SEM) using an energy dispersive X-ray (EDX) detector (Zeiss Auriga) was used to map surface morphology and elemental composition. UV-Vis-NIR spectroscopy using a Schimadzu 3100 spectrophotometer and Fourier Transform Infrared Spectroscopy (FTIR) (BRUKER Alpha II)

were used to optical characterization of the samples. The electrical measurements were collected using an Agilent 4294A analyzer for impedance spectroscopy of samples in the frequency range of 40 Hz-110 MHz, as well as a Janis VPF800 cryostat to change the temperature from 120 to 500 K. This experiment used an alternating current signal with an amplitude of 0.05 V. The current-voltage curves were obtained at temperatures ranging from 80 K to 500 K with a Keithley 220 current generator and an Agilent 3400 voltmeter.

3. Results and discussion

3.1. Structural properties

Fig.3 presents the X-ray diffraction (XRD) patterns of $Cd_{0.7}Fe_{2.3}O_4$ ferrite thin films before and after annealing at different temperature. No diffraction peaks are observed in the as-deposited film, indicating its amorphous nature. After annealing, distinct diffraction peaks appear, with the most intense peak located at 2θ = 34.71°, 34.63° and 33.31° for thin films annealed at 600 °C, 750 °C and 900 °C, respectively, corresponding to the (311) plane. This peak is attributed to the characteristic reflection of spinelle ferrites [15].

All diffraction peaks were indexed according to the JCPDS card no. 22-1063, confirming the formation of a cubic spinel structure with space group $Fd\bar{3}m$ [16]. The peak intensity increases and its width decreases with increasing annealing temperature. This trend indicates a significant improvement in crystallinity. Moreover, weak traces of characteristic peaks are detectable in the as-deposited film. This suggests that crystallization begins during the deposition step. These results demonstrate that spinel ferrite thin films can be successfully obtained by spray pyrolysis under appropriate preparation and annealing conditions.

The average crystallite size (D) was estimated using the Debye-Scherrer formula [17] applied to the most intense peak (311). The equation for crystallite size estimation is given by:

$$\boldsymbol{D = \frac{k.\lambda}{\beta \cos \theta}} \quad \textbf{(2)}$$

where λ is the wavelength of Cu kα radiation (1.5406 Å), θ is the Bragg angle, β is the full-width at half maximum (FWHM) and k is a dimensionless form factor with a value of approximately

0.9. The average crystallite size is approximately 14 nm at 600 °C, increasing to 25 nm at 750 °C and 32 nm at 900 °C. This increase confirms grain growth and improved crystallinity with increasing annealing temperature.

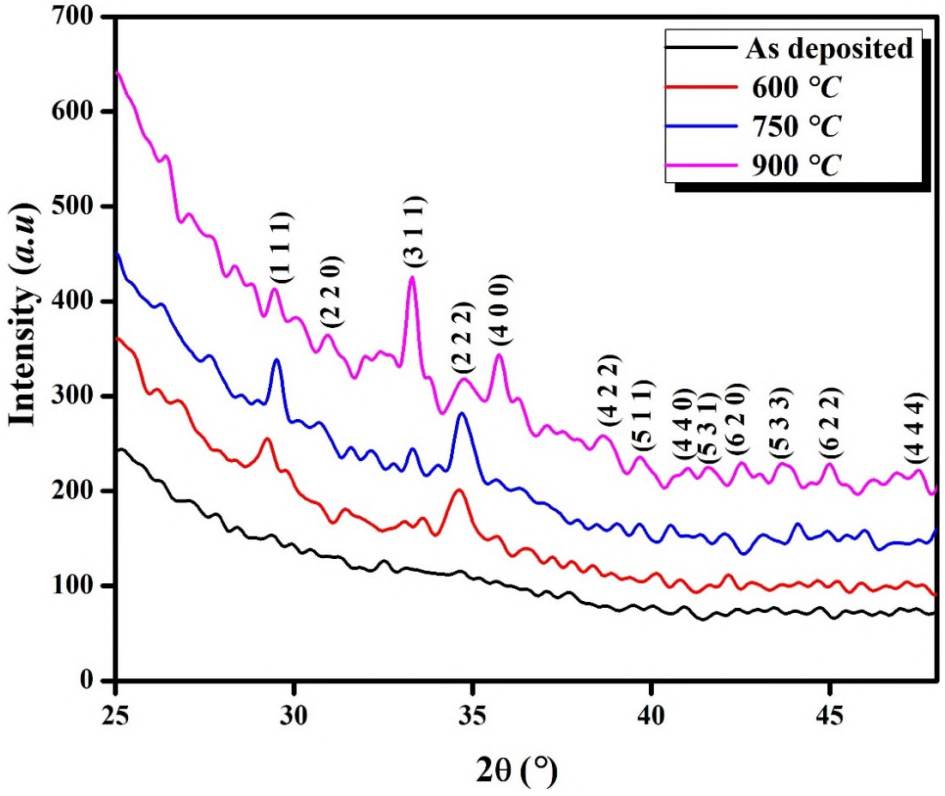


Fig. 3: XRD patterns of $Cd_{0.7}Fe_{2.3}O_4$thin films calcined at 600°C, 750°C and 900°C.

3. 2. EDX and SEM analysis

Energy-dispersive X-ray (EDX) spectroscopy was used to determine the elemental composition of $Cd_{0.7}Fe_{2.3}O_4$ thin films. **Fig. 4a** shows the EDX spectrum of the as-deposited film. The spectrum confirms the presence of Cd, Fe, and O, each associated with characteristic X-ray peaks, indicating the formation of the expected compound. Elemental mapping of the $Cd_{0.7}Fe_{2.3}O_4$ film was performed using SEM coupled with EDX, as shown in **Fig. 4b–d**. This analysis reveals a homogeneous distribution of all elements throughout the cadmium ferrite film. Each element is represented by a distinct color in the maps: iron (yellow), cadmium (green), and

oxygen (red) (**Fig. 4b–d**). These results confirm that the spray pyrolysis process enables the deposition of homogeneous ferrite thin films without detectable contamination.

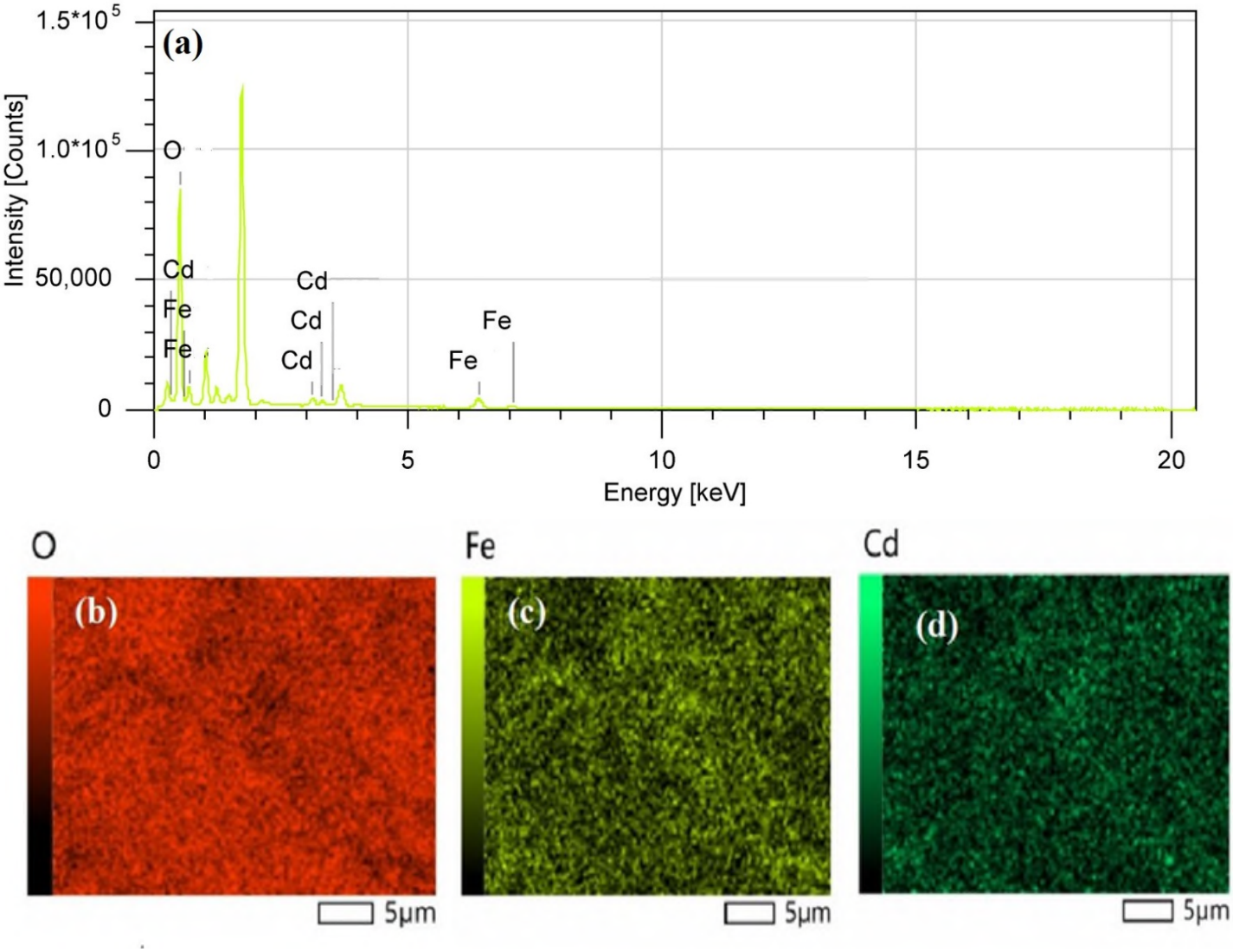


Fig. 4: **a)** EDX spectrum showing the presence of different element without any supplemental impurities. Elemental **b**, **c** and **d** mapping images illustrating O (red dots) Fe (yellow dots) and Cd (green dots).

Fig. 5 depicts cross-sectional view of $Cd_{0.7}Fe_{2.3}O_4$ films without annealing obtained with SEM. It can be observed that the deposited layer is compact and adheres to the substrate. The film thickness is approximately 1.6 µm.

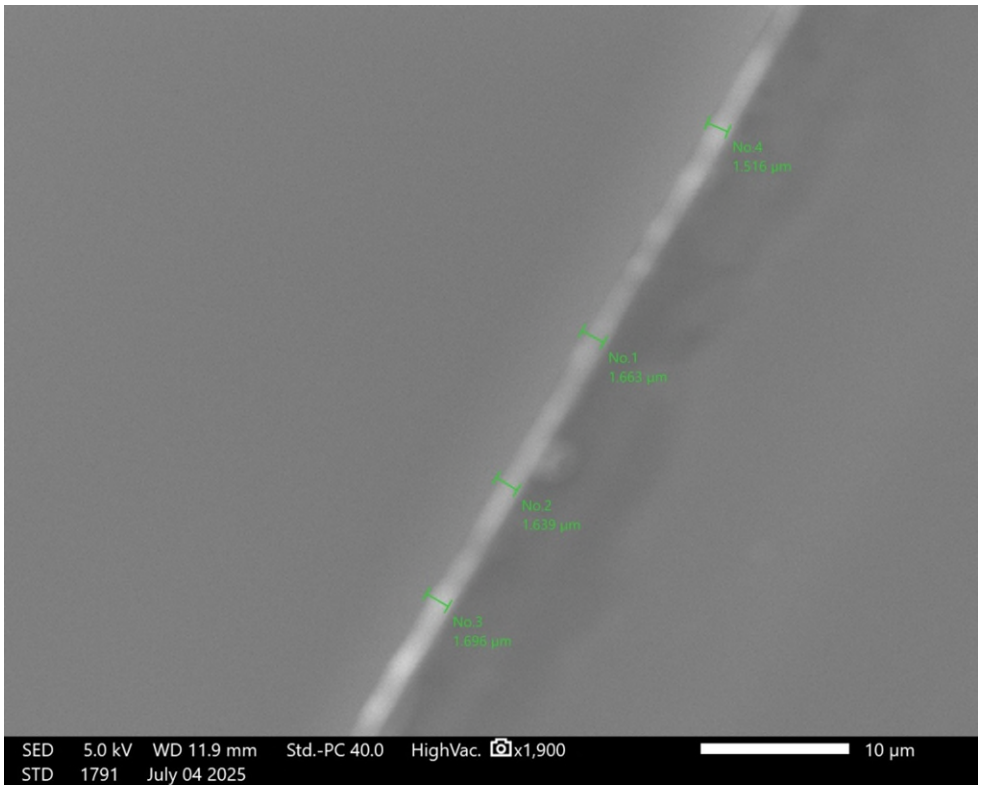
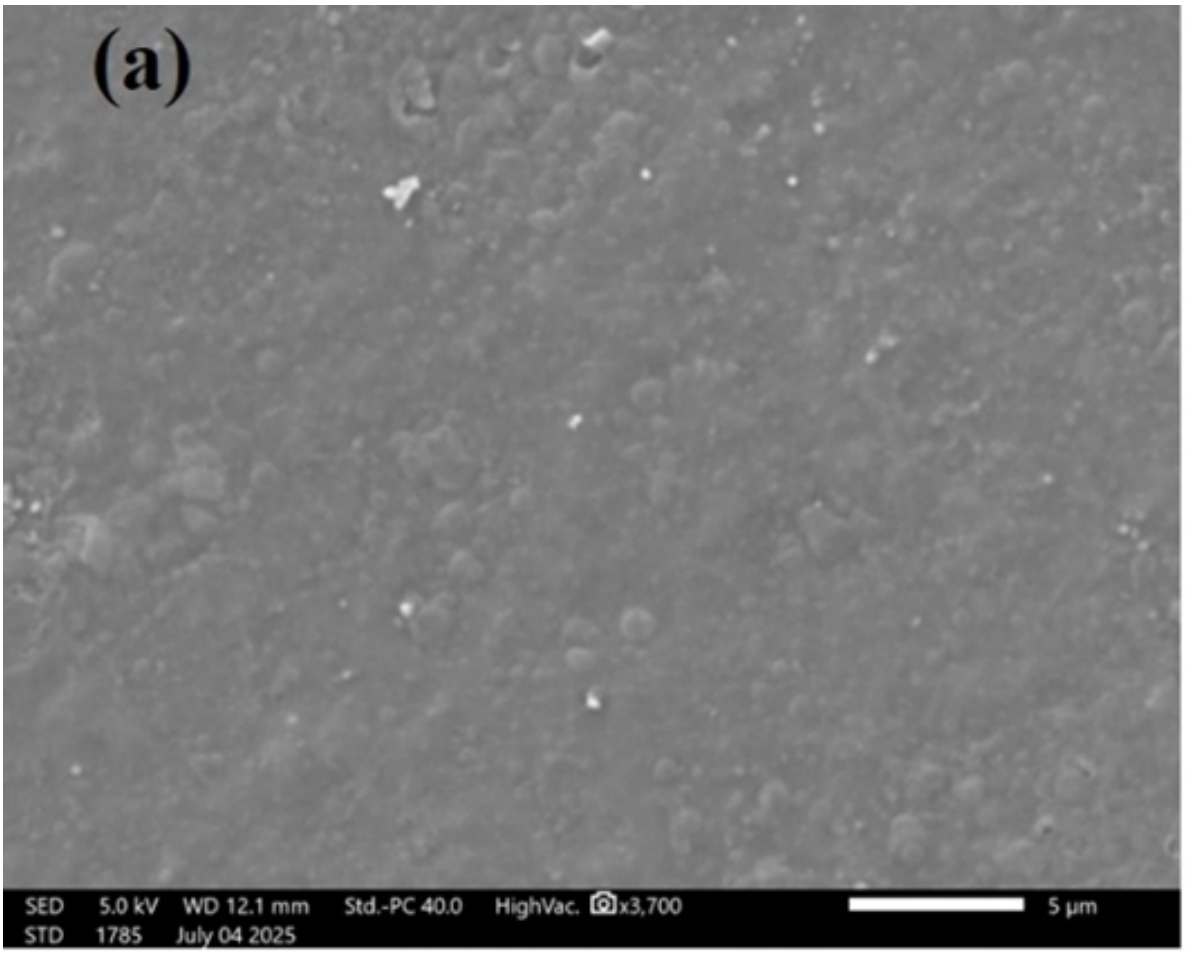


Fig. 5: cross-sectional view SEM micrographs for $Cd_{0.7}Fe_{2.3}O_4$ thin films.

The structure and morphology of the $Cd_{0.7}Fe_{2.3}O_4$film were visualized using SEM. The obtained image is shown in **Fig. 6a.** The photo indicates that the layer is thoroughly homogenous and compact. The average grain size estimated from the SEM picture is around 0.7 µm (**Fig. 6b**). these results are very encouraging. They evidence that it is possible to obtain a pure, homogenous, compact and crystallized thin film of $Cd_{0.7}Fe_{2.3}O_4$ with a low-cost, and flexible technique.



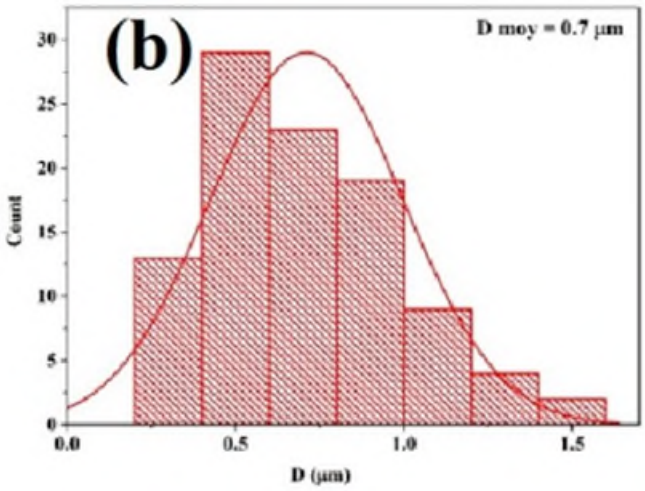


Fig. 6: **a)** SEM image and b) grain size distribution plot.

3. 3. Optical analysis

3. 3. 1. FTIR analysis

Bulk cadmium ferrite is classified as a typical spinel ferrite based on the distribution of iron and cadmium ions between tetrahedral (A) and octahedral (B) sites [18,19]. Fourier transform infrared (FTIR) spectroscopy was performed to identify the characteristic metal–oxygen bonds in the prepared thin films. The resulting spectra are shown in **Fig. 7**, where the inset corresponds to an enlarged view of the as-deposited film. Similar spectral features have been reported in previous studies [20–22]. **Fig. 7** also shows the FTIR spectrum of the quartz substrate for comparison. A clear difference is observed between the spectrum of the bare quartz substrate and that of the ferrite-coated sample. The spectrum of pure quartz is dominated by a broad absorption band in the range 500-2000 cm^{-1}. In contrast, the coated samples exhibit additional absorption bands that are absent in the bare quartz spectrum, indicating the formation of new chemical bonds associated with the deposited material. Three prominent peaks at 931, 812, and 579 cm^{-1} are attributed to metal-oxygen vibrations corresponding to Cd-O and Fe-O bonds [23]. The bands at 1617 and 1344 cm^{-1} are assigned to Cd-O-Fe linkages, confirming the formation of the ferrite structure [24]. These results provide further evidence for the successful deposition of the desired ferrite layer. As the annealing temperature increases, both the intensity and position of certain peaks change significantly. These variations are attributed to structural modifications within the films, including densification and defect reduction…

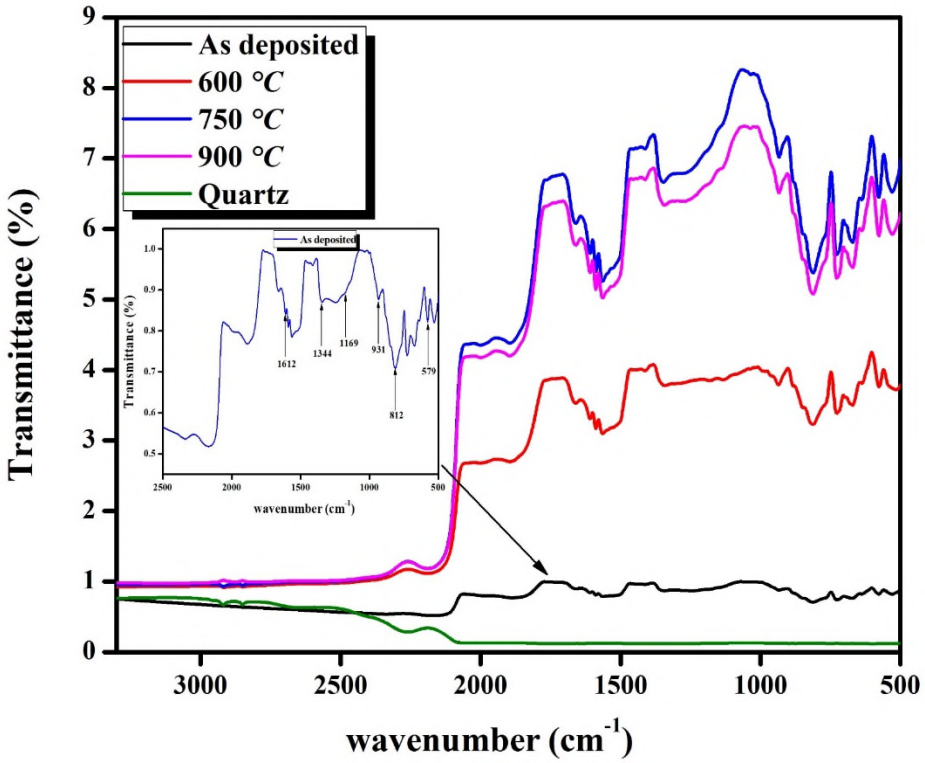


Fig. 7*:* FTIR spectrum of the quartz substrate and the layer at different annealing temperatures.

3. 3. 2. UV-Visible-NIR analysis

Fig. 8a shows the transmittance spectra of the $Cd_{0.7}Fe_{2.3}O_4$ thin films before and after annealing over the wavelength range 200 - 3100 nm. The films exhibit strong absorption in the UV-visible region, indicating their suitability for energy conversion applications [25,26]. In addition, a clear dependence of the transmittance on annealing temperature is observed, which can be attributed to changes in surface morphology, crystallite size, and structural disorder that influence light scattering [27]. The increase in transmittance with annealing is associated with improved surface smoothness and reduced defect density. The decrease observed at 900 °C may be attributed to film densification, which enhances light absorption. The bandgap energy was determined using the Tauc relation for allowed direct transitions (**Fig. 8b**) [28]:

$$(\alpha d h\vartheta)^2 = C\left(h\vartheta - E_g\right) \quad (3)$$

where $h\vartheta$ is the photon energy, E_g is the bandgap energy, C is a non-frequency dependent constant, and α is the absorption coefficient. The absorption coefficient was calculated using ($\alpha = \frac{1}{d}\ln\frac{1}{T}$).

The obtained bandgap values range between 2.13 and 2.91 eV. $Cd_{0.7}Fe_{2.3}O_4$ thin films exhibit a systematic increase in optical band gap with increasing annealing temperature, which correlates with the improvement in crystallinity evidenced by the reduction in XRD peak width and increase in peak intensity. This correlation indicates that the optical evolution is primarily governed by structural relaxation rather than phase transformation, since no secondary phases are detected in XRD patterns. This behavior is typical of spinel oxides, where electronic properties are strongly influenced by cationic disorder and defect density. Thus, the observed bandgap increase can be considered intrinsic to the $Cd_{0.7}Fe_{2.3}O_4$ spinel phase, in agreement with models describing non-stoichiometric ferrites. At low deposition temperatures, the films exhibit high structural disorder and contain a high density of point defects, including oxygen vacancies (V_O), Fe^{2+}/Fe^{3+} centers and cation distribution disorder between tetrahedral and octahedral sites. These defects introduce localized electronic states within the band gap, leading to significant sub-gap absorption. This results in an apparent narrowing of the optical band gap, as widely observed in disordered transition metal oxides [29]. The increase in band gap with annealing can be attributed to several mechanisms: (i) reduction of oxygen vacancies due to reoxidation, (ii) stabilization of Fe^{3+} ions, which reduces polaronic transitions, and (iii) improved cation ordering within the spinel lattice. These effects decrease defect-related states and enhance band edge definition. At an annealing temperature of 900 °C, the band gap decreases to approximately 2.13 eV, which is consistent with reported values in the literature [30], suggesting the stabilization of a modified or secondary phase.

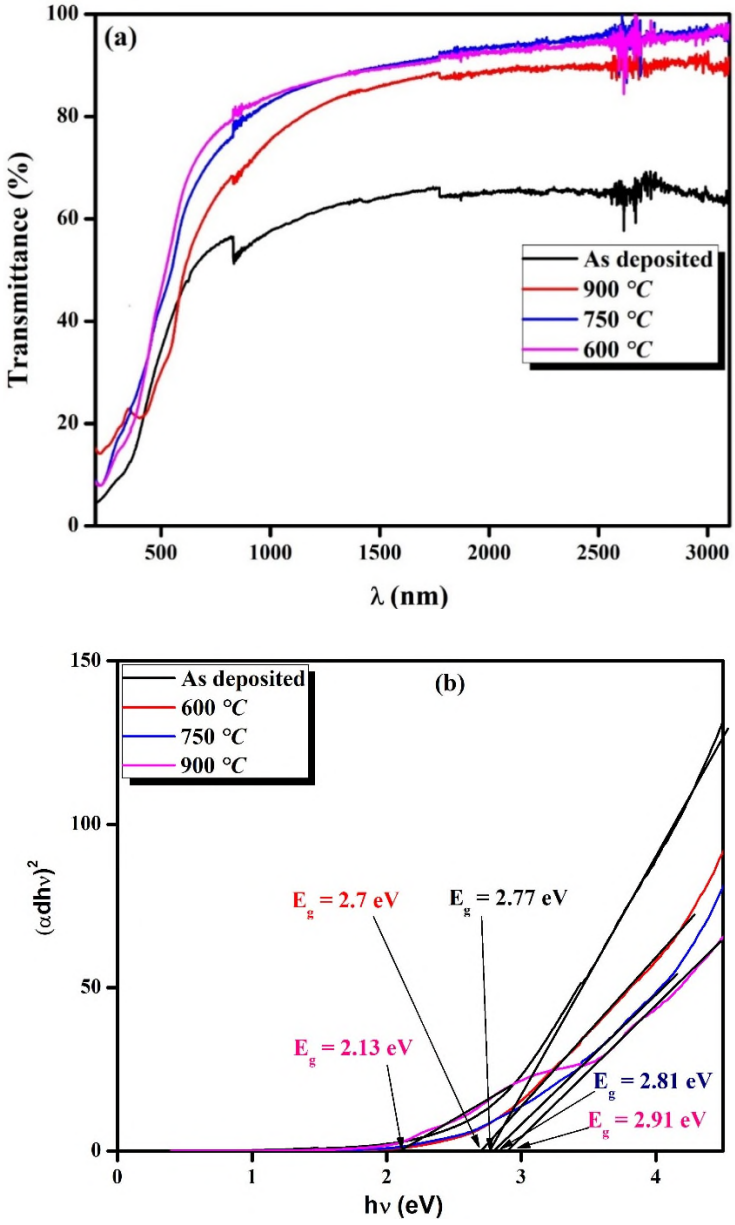


Fig. 8: **a)** Transmittance measurements for $Cd_{0.7}Fe_{2.3}O_4$ before and after treatment, **b)** Tauc-plot.

3.4. Electrical results

3. 4. 1. Conductance study

Fig. 9 shows the frequency dependence of the conductance of $Cd_{0.7}Fe_{2.3}O_4$ thin films deposited on an indium tin oxide (ITO) substrate at room temperature. The conductance is approximately 5.10^{-2} S at low frequency and decreases with increasing frequency, indicating that the conduction mechanism is not purely metallic.

The frequency-dependent conductance may be described using the Drude model [31]:

$$G(w) = \frac{G_0}{(1+\omega^2\tau^2)} \quad (4)$$

where τ is the characteristic relaxation time. The estimated value of τ is on the order of 10^{-7} s. This value is significantly higher than typical electron scattering times predicted by the classical Drude model. It reflects a dielectric relaxation process governed by hopping conduction between Fe^{2+}/Fe^{3+} ions and Maxwell-Wagner interfacial polarization at grain boundaries. Such long relaxation times are characteristic of polycrystalline spinel ferrites, where charge carriers are strongly localized and transport is dominated by thermally activated hopping and interfacial barrier effects rather than free-electron conduction [32,33].

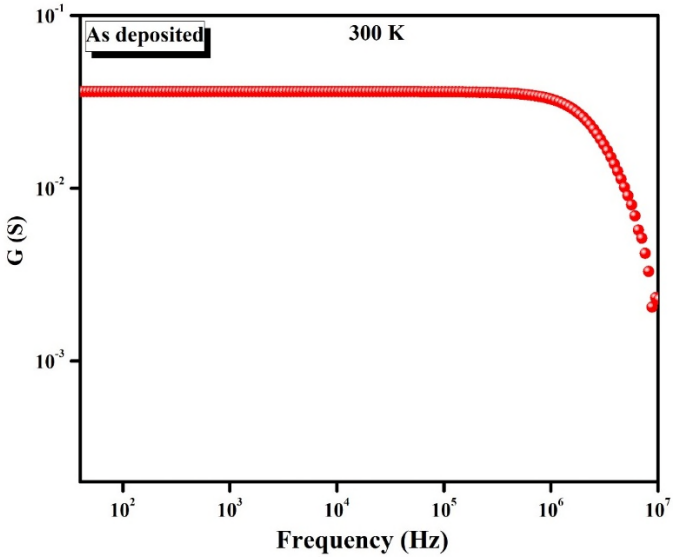


Fig. 9: Variation of conductance with frequency at 300 K for $Cd_{0.7}Fe_{2.3}O_4$ deposited on ITO substrate.

Fig. 10 shows the conductance spectra of the Ag/$Cd_{0.7}Fe_{2.3}O_4$/N-Si/Ag heterostructure measured over the temperatures range 120-500 K. The spectra exhibit two dispersion regions and two frequency-independent regions, indicating multiple conduction mechanism.

Based on the results presented in **Fig. 9**, the ferrite layer behaves as a highly conductive material. Furthermore, considering the deposition conditions, the formation of a thin SiO_2 layer at the ferrite/silicon interface is unavoidable. Therefore, the device can be modeled as a heavily doped semiconductor/insulator/semiconductor (S/I/S) structure, namely $Cd_{0.7}Fe_{2.3}O_4/SiO_2$/N-Si.

The observed frequency-dependent conductance arises from several contributions: (i) interface states at the Si/SiO_2 boundary, (ii) series resistance associated with the ferrite and silicon layers, (iii) interface states at the SiO_2/ferrite junction, and (iv) relaxation phenomena within the ferrite layer, such as charge trapping–detrapping and interfacial polarization processes [34].

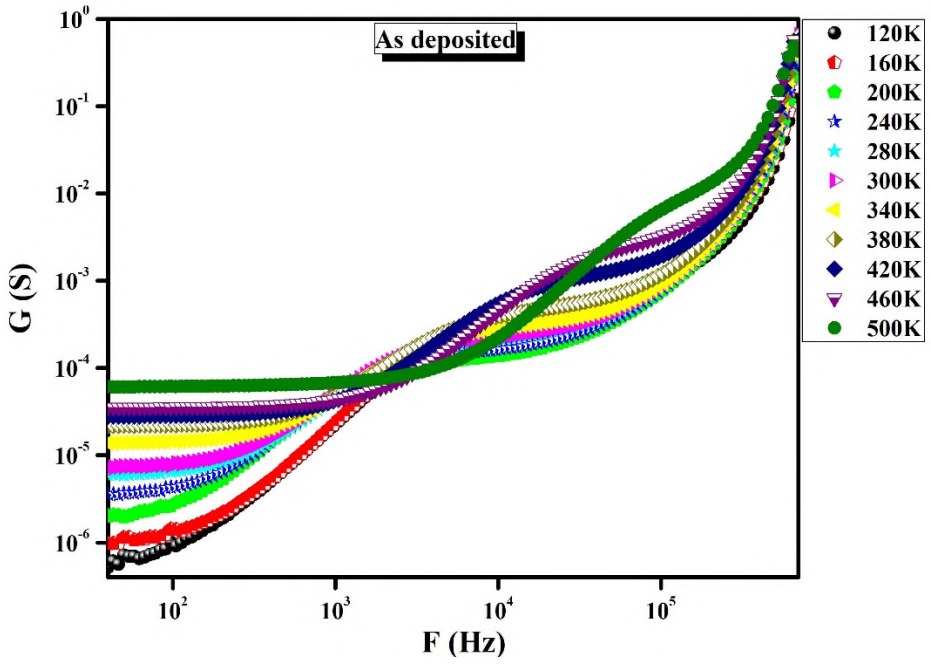


Fig. 10: Conductance variation with frequency at various temperatures for Ag/$Cd_{0.7}Fe_{2.3}O_4$/N-Si/Ag heterostructure.

Cadmium ferrite ($CdFe_2O_4$) is a spinel oxide semiconductor whose electrical properties are strongly governed by cation distribution, defect chemistry, and synthesis conditions. Density

functional theory (DFT) studies indicate that $CdFe_2O_4$ exhibits a relatively narrow band gap with semiconductor behavior [35] . However, as in most spinel ferrites, the dominant carrier type is not intrinsic but controlled by defects. In spinel ferrites (MFe_2O_4), electrical transport is generally dominated by small polaron hopping between Fe^{2+} and Fe^{3+} ions. The type and concentration of charge carriers depend sensitively on intrinsic defects such as cation vacancies, anti-site defects, and oxygen vacancies. First-principles studies have demonstrated that growth conditions strongly influence the conduction type: oxygen-rich (metal-poor) environments favor the formation of cation vacancies acting as shallow acceptors, leading to p-type conductivity, whereas oxygen-deficient or metal-rich conditions promote oxygen vacancies, which act as donors and result in n-type behavior [36]. More generally, it is well established that synthesis parameters—including thermal treatment, atmosphere, and precursor chemistry—play a key role in determining the electrical properties of spinel ferrites [37]. In particular, wet-chemical methods such as sol–gel or co-precipitation often lead to non-equilibrium defect populations, including cation deficiency and excess iron. In this context, non-stoichiometric compositions such as $Cd_{0.7}Fe_{2.3}O_4$ (Fe-rich ferrite) are expected to deviate significantly from the ideal spinel structure. The excess iron content may induce (i) Cd^{2+} vacancies acting as acceptors, (ii) an increased Fe^{3+} concentration enhancing hole hopping pathways, and (iii) redistribution of cations between tetrahedral and octahedral sites. Such defect configurations are consistent with those observed in other Fe-rich spinel systems, where acceptor-type defects promote hole conduction. Experimental evidence from related materials supports this interpretation. For example, p-type conductivity has been reported in spinel ferrites such as $GeFe_2O_4$, where holes are identified as the majority carriers, as well as in non-stoichiometric ferrite thin films with cation excess [38]. Therefore, although stoichiometric $CdFe_2O_4$ is not systematically classified as p-type, the combined effects of (i) Fe-rich non-stoichiometry (Cd deficiency), (ii) oxidizing growth conditions, and (iii) defect-induced acceptor states strongly suggest that $Cd_{0.7}Fe_{2.3}O_4$ exhibits predominantly p-type semiconducting behavior, governed by hole hopping between Fe^{3+}/Fe^{2+} states. This hypothesis is consistent with the general defect physics of spinel ferrites and will be further supported by the rectifying behavior observed in the current-voltage characteristics discussed in the next section. Accordingly, the conductance spectrum at 340 K (**Fig. 11**) can be interpreted within the framework of a p–i–n-type heterostructure.

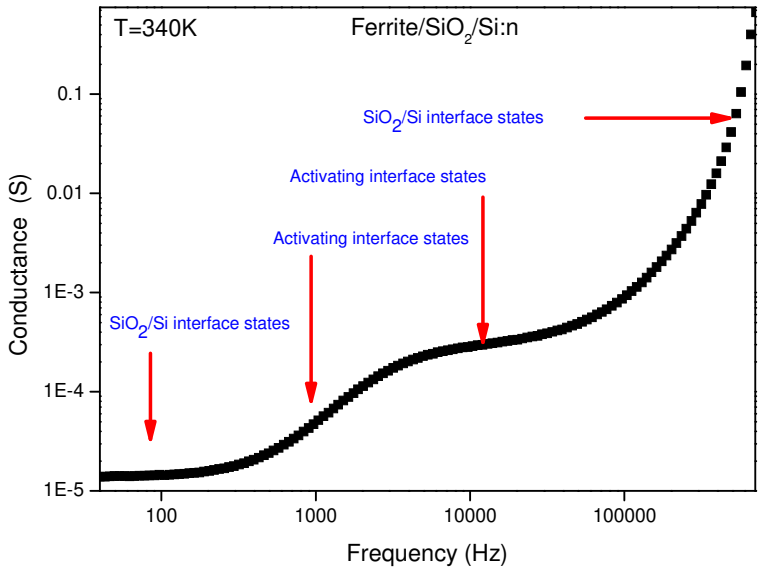


Fig. 11: Analysis of the different branches of the conductance spectrum of $Cd_{0.7}Fe_{2.3}O_4/SiO_2/Si$-n structure (recorded at 340K).

The low-frequency plateau (approximately 10^2 Hz – 10^3 Hz), characterized by low and nearly constant conductance, can be attributed to slow interface states at the SiO_2/Si interface. These states are associated with deep trap levels possessing long relaxation times, allowing them to follow the low-frequency AC signal.

As the frequency exceeds 10^3 Hz, these interface states become increasingly unable to respond to the alternating signal, leading to an increase in conductance. Around 10^4 Hz, a second quasi-stable plateau with higher conductance is observed. This behavior is attributed to the saturation of fast interface states and is commonly reported in admittance spectroscopy of Metal/Insulator/Semiconductor (MIS) and p^+–i–n structures. A second dispersion zone appears around 10^5 Hz. This feature can be explained by interfacial polarization effects, particularly charge accumulation at the interfaces of the heterogeneous structure. In such systems, the coexistence of conductive and insulating layers gives rise to Maxwell–Wagner polarization.

The contribution of electronic hopping conduction between Fe^{2+} and Fe^{3+} ions in the ferrite layer can be excluded, as no similar dispersion behavior is observed in the conductance spectrum of the ferrite alone (**Fig. 9**).

3. 4. 2. Characteristic current-voltage (I (V))

Fig. 12 presents the current-voltage (I-V) characteristics of the $Cd_{0.7}Fe_{2.3}O_4/SiO_2/Si$: N structure measured at different temperatures. The I–V curves exhibit clear rectifying behavior, characteristic of a p^+–n heterojunction incorporating an insulating interfacial layer. The strong temperature dependence of the current indicates that charge transport is primarily governed by thermally assisted mechanisms, such as thermionic emission over the potential barrier, combined with trap-assisted tunneling through the SiO_2 layer and interface states. Furthermore, the deviation from ideal diode behavior, including the absence of a well-defined reverse saturation current, suggests the presence of barrier inhomogeneities and a high density of interface states. Such features are typical of ferrite-based p^+–i–n structures, where interfacial effects and defect states play a dominant role in charge transport.

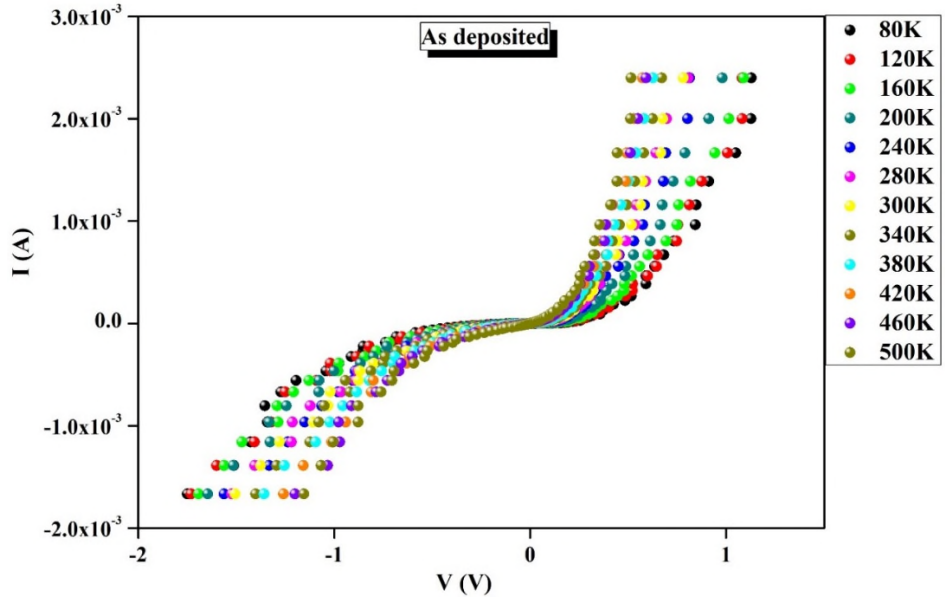


Fig. 12: I-V-T characteristic of the $Cd_{0.7}Fe_{2.3}O_4/SiO_2/Si$: N heterostructure.

The current–voltage characteristics were modeled using MATLAB software based on the Shockley diode equation [39]:

$$\boldsymbol{I = I_S \left[\exp\left(\frac{q(V-R_S I)}{nk_B T}\right) - 1\right]} \quad \textbf{(5)}$$

where k_B is the Boltzmann constant, T is the absolute temperature, n is the ideality factor, Rs is the series resistance, I_s is the saturation current, q is the elementary charge, and V is the applied voltage. **Fig. 13** compares the experimental I-V characteristics with the simulated curves at different temperatures. A good agreement is observed over the entire voltage range, indicating that the model accurately reproduces the electrical behavior of the heterostructure. These results confirm that the modified Shockley equation, incorporating series resistance, provides an appropriate framework for describing the transport mechanisms in the $Cd_{0.7}Fe_{2.3}O_4/SiO_2$/n-Si device.

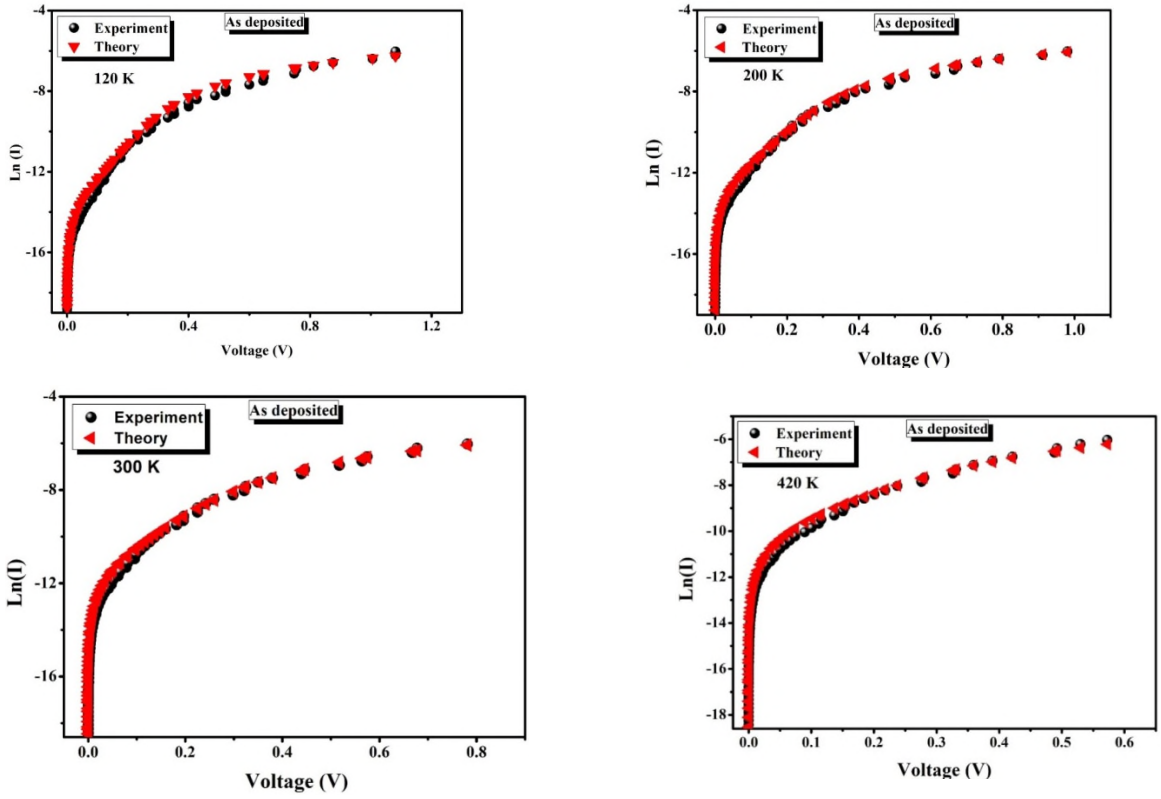


Fig. 13: Theoretical and experimental I-V measured at different temperatures.

The variation of the ideality factor as a function of temperature is presented in Figure 14. The ideality factor decreases significantly with increasing temperature, from 6.65 at 80 K to 1.49 at 500 K. At low temperatures, the high values of the ideality factor indicate strong deviations from ideal diode behavior. This can be attributed to non-ideal transport mechanisms such as tunneling (field emission), as well as the presence of barrier inhomogeneities, interface defects, and the influence of series resistance [40]. As the temperature increases, charge carriers gain sufficient thermal energy to overcome the potential barrier through thermionic emission. This transition toward thermally activated transport reduces the contribution of tunneling and interface-related effects, leading to a decrease in the ideality factor [41]. At higher temperatures, the ideality factor approaches values closer to unity, indicating a more ideal diode behavior dominated by thermionic emission.

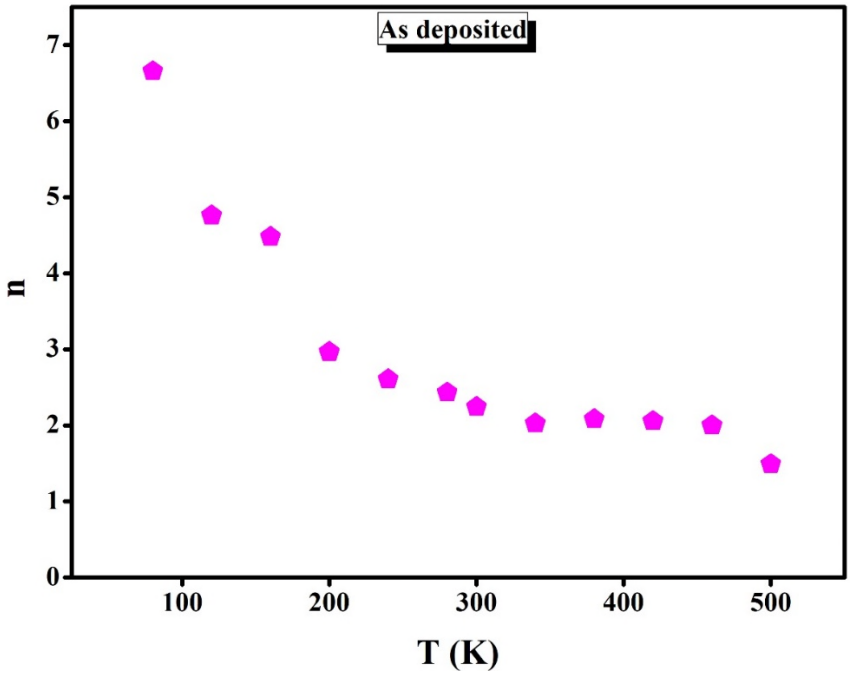


Fig. 14: Ideality factor (n) as a function of temperature.

Fig.15 shows the variation of the series resistance (Rs) as a function of temperature. The results indicate a significant decrease in Rs with increasing temperature, from 411 Ω at 80 K to 120 Ω at 500 K. This behavior can be attributed to the increase in charge carrier energy at higher

temperatures, which enhances carrier mobility and reduces resistive losses within the structure. As a result, charge transport becomes more efficient, leading to a decrease in the overall series resistance. Moreover, the series resistance is influenced by the combined contributions of the ferrite layer, the interfacial SiO_2 layer, and the n-type silicon substrate. The temperature dependence of Rs therefore reflects the improved conductivity of these layers and the reduction of barrier effects at elevated temperatures.

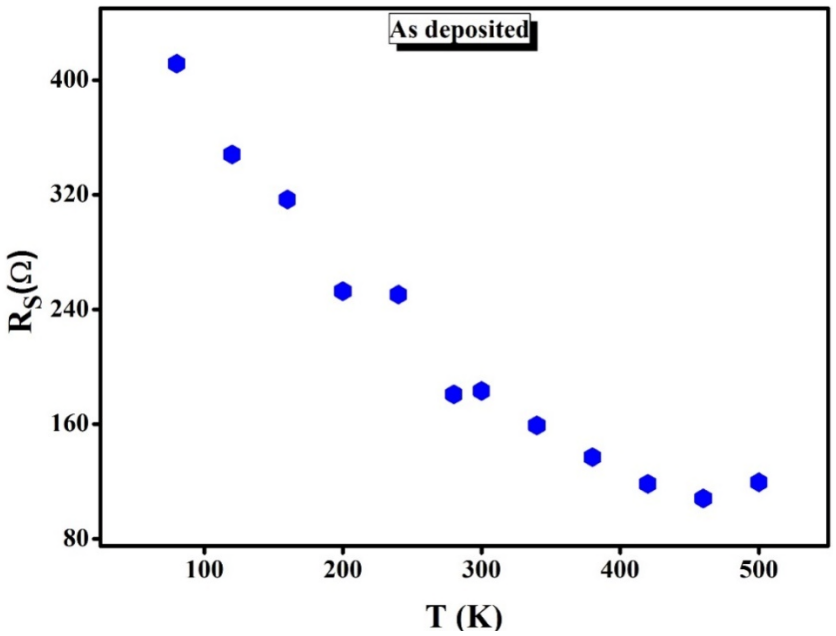


Fig. 15: Series resistance (Rs) as a function of temperature.

The variation of the saturation current (Is) with temperature is presented in **Fig. 16**. The results show that Is increases significantly from 2.11×10^{-7} A at 80 K to 1.81×10^{-5} A at 500 K. This increase can be attributed to the enhanced thermionic emission of charge carriers over the potential barrier as temperature rises. At higher temperatures, carriers acquire sufficient thermal energy to overcome the barrier more easily, leading to an increase in the saturation current. Additionally, small fluctuations observed around 200 K may be associated with the contribution of interface states, which can influence carrier transport through trapping and detrapping mechanisms.

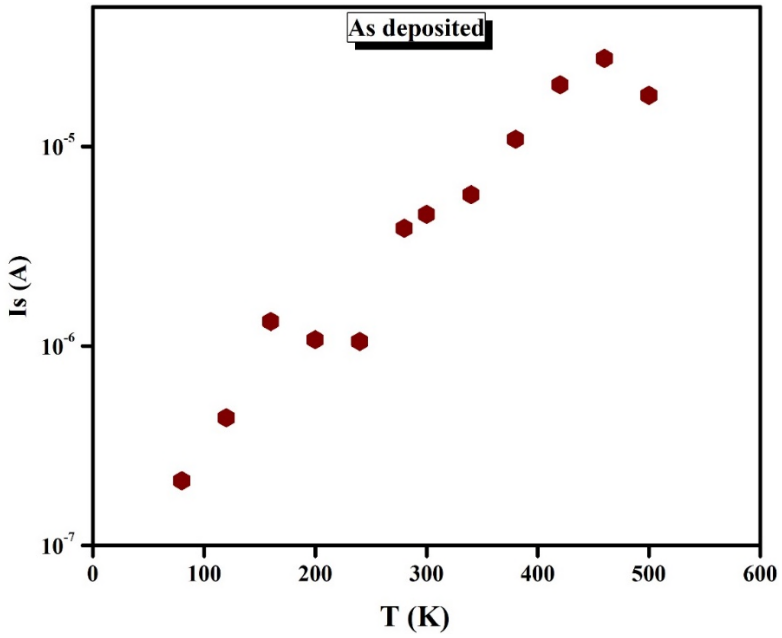
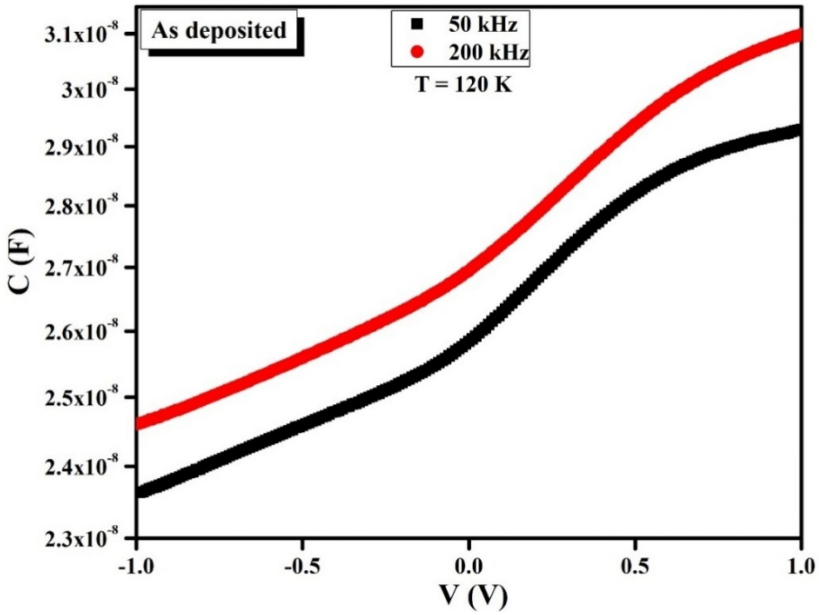
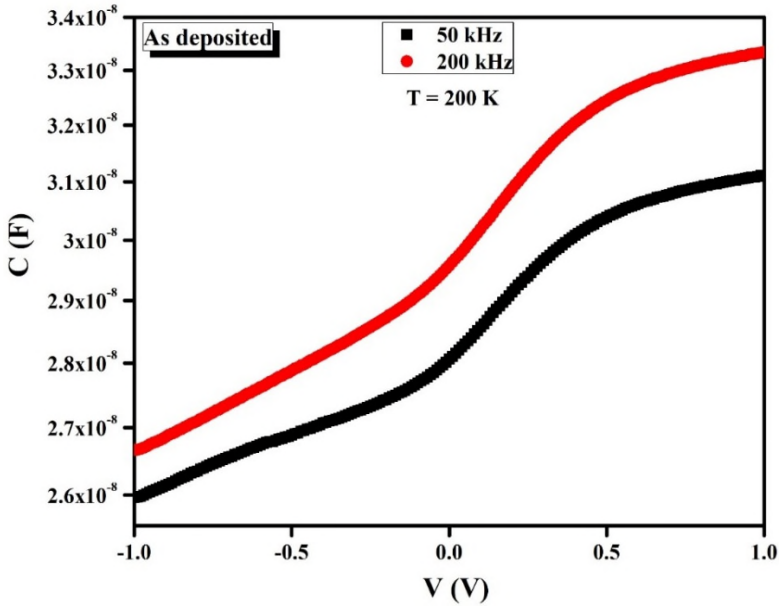


Fig. 16: Saturation current intensity (Is) as a function of temperature.

3. 4. 3: Characteristic capacitance-voltage (C(V))

Fig. 17 shows the variation of the capacitance of the heterostructure as a function of bias voltage at different temperatures and frequencies. The results indicate that the capacitance increases with measurement frequency. This behavior can be attributed to the limited ability of charge carriers and interface states to follow the applied AC signal at high frequencies. As a result, the contribution of slow states is reduced, leading to a decrease in the effective depletion width and a corresponding increase in capacitance. Moreover, the capacitance is found to increase with temperature. This trend is associated with the thermal activation of charge carriers, which enhances their contribution to polarization and charge accumulation within the structure. This behavior is consistent with the temperature dependence observed in the conductance and current–voltage characteristics. In the following, the C–V characteristic at 50 kHz and 300 K is analyzed in detail, conditions under which the assumption of fully ionized centers is more valid.


As deposited
50 kHz
200 kHz
T = 120 K
C (F)
V (V)
3.1x10-8
3x10-8
2.9x10-8
2.8x10-8
2.7x10-8
2.6x10-8
2.5x10-8
2.4x10-8
2.3x10-8
-1.0
-0.5
0.0
0.5
1.0


As deposited
50 kHz
200 kHz
T = 200 K
C (F)
V (V)
3.4x10-8
3.3x10-8
3.2x10-8
3.1x10-8
3x10-8
2.9x10-8
2.8x10-8
2.7x10-8
2.6x10-8
-1.0
-0.5
0.0
0.5
1.0

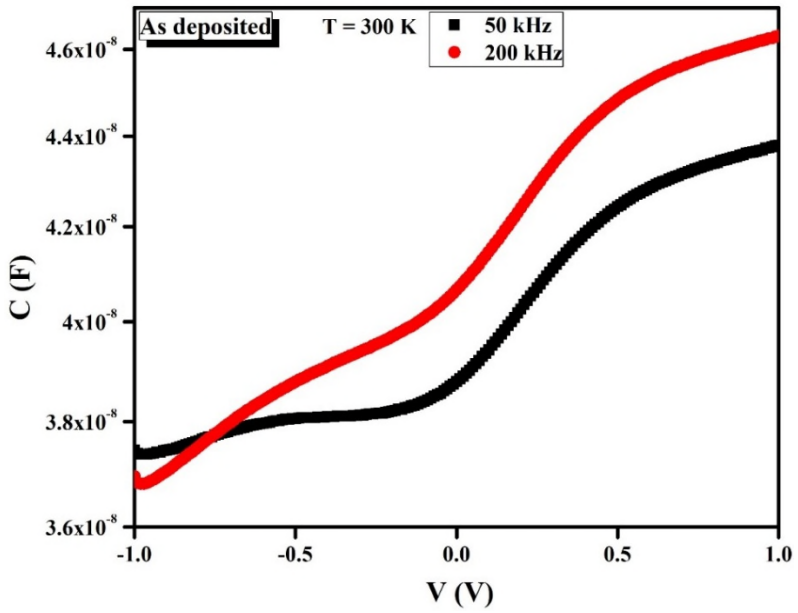


Fig. 17: Capacitance-voltage characteristic at different frequencies and temperatures.

Mott-Schottky analysis was performed to extract key semiconductor parameters from the C-V measurements. **Fig. 18** shows the variation of C^{-2} as a function of the applied voltage. The linear behavior observed in this plot confirms the validity of the depletion approximation and indicates a well-defined space charge region.

The relationship between capacitance and voltage is given by [42]:

$$\frac{1}{C^2} = \frac{2}{qN_D S^2 \varepsilon_{sc} \varepsilon_0}(V - V_d) \quad (6)$$

where ε_{sc} is the semiconductor permittivity, ε_0 is the vacuum permittivity, S is the junction area, N_D is the donor concentration, q the elementary charge, V_d is the built-in (diffusion) potential, and V is the applied voltage.

From the slope of the linear region ($\frac{2}{qN_D S^2 \varepsilon_{sc} \varepsilon_0}$) , the donor concentration was estimated to be on the order of $8.7.10^{17}$ cm^{-3}. The intercept of the linear fit with the voltage axis yields a diffusion potential V_d of approximately 0.7 V.

These values are consistent with moderately doped semiconductor behavior and support the electrical analysis of the heterostructure.

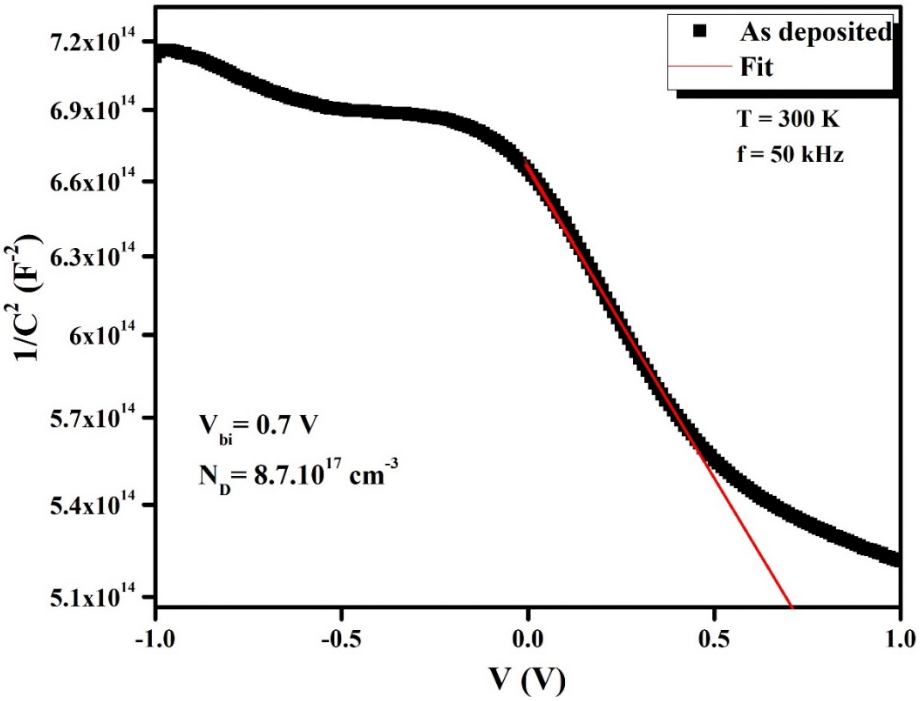


Fig. 18: Mott-Schottky plot (50 kHz) of our heterostructure at room temperature.

These values are typical of Si: N bulk material. This confirms that the ferrite layer is heavily doped and the space charge area expansion with reverse polarization takes place in silicon.

4. Summary and final remarks

In this work, $Cd_{0.7}Fe_{2.3}O_4$ thin films were successfully deposited by the spray pyrolysis technique, demonstrating the reliability of this simple and cost-effective method for the fabrication of functional oxide materials. A systematic investigation of the annealing temperature revealed its critical role in enhancing the structural, morphological, and optical properties of the films. X-ray diffraction confirmed the formation of a single-phase cubic spinel structure after annealing, accompanied by a significant improvement in crystallinity and an increase in crystallite size from 14 to 32 nm. SEM and EDX analyses evidenced homogeneous, dense films

with compositions close to the target stoichiometry and free from detectable impurities. Optical and FTIR measurements confirmed the formation of cadmium ferrite and revealed strong absorption in the UV–visible region, with an optical band gap varying from 2.13 to 2.91 eV depending on annealing conditions. The electrical behavior of the $Cd_{0.7}Fe_{2.3}O_4$/n-Si heterostructure, including the presence of an interfacial SiO_2 layer, was thoroughly analyzed. The ferrite layer was identified as a heavily p-type semiconductor, leading to the formation of a p^+–i–n-type junction. Conductance spectroscopy revealed multiple contributions arising from interface states, series resistance, and interfacial polarization mechanisms. Current–voltage measurements exhibited clear rectifying behavior with strong temperature dependence, well described by a modified Shockley model including series resistance. The extracted parameters (ideality factor, saturation current, and series resistance) are consistent with conduction mechanisms dominated by thermionic emission and defect-assisted transport. Capacitance–voltage analysis confirmed the junction behavior and enabled the extraction of key semiconductor parameters, including a diffusion potential of approximately 0.7 V and a carrier concentration on the order of 1018 cm^{-3}, indicating a heavily doped ferrite layer. Overall, this study demonstrates the feasibility of fabricating ferrite/silicon heterojunctions with tunable properties suitable for electronic and optoelectronic applications. Future work should focus on controlling the interfacial SiO_2 layer, either by minimizing its thickness or by exploiting its presence in engineered device architectures.

CRediT authorship contribution statement

Mootez Smiti: Investigations, data curation, Formal analysis, Writing – original draft. **Sabrine Mourad:** data curation, Formal analysis, Writing – original draft, **Rehab Ramadan Shehata Ali:** investigations, Formal analysis, Validation, Writing – review & editing, **Raúl José Martín-Palma:** Conceptualization Supervision, Validation, Writing – review & editing, **Ahmed Slimani:** investigations, **,** Formal analysis, Writing – review & editing, **Omayma Amorri:** investigations, Formal analysis, Writing – review & editing, **Faysal Tiss:** Formal analysis, Validation, Writing – review & editing, **Kamel Khirouni:** Supervision, Methodology, Funding acquisition, Writing – review & editing, Writing –Conceptualization. **Essebti Dhahri:** Supervision, Methodology, Funding acquisition, Writing – review & editing, Conceptualization

.

Declaration of competing interest

The authors declare that they have no known competing financial interests or personal relationships that could have appeared to influence the work reported in this paper.

Acknowledgements

This work was supported the Tunisian Ministry of High Education and Scientific Research through funding allowed to the implied Labs.

Data availability

Data will be made available on request.

References

1. H. J. Kardile, S. B. Somvanshi, A. R. Chavan, A. A. Pandit, and K. M. Jadhav, Optik **207**, 164462 (2020).

2. N. Y. Mostafa, Z. I. Zaki, and Z. K. Heiba, Journal of Magnetism and Magnetic Materials **329**, 71 (2013).

3. V. Vasanthi, A. Shanmugavani, C. Sanjeeviraja, and R. Kalai Selvan, Journal of Magnetism and Magnetic Materials **324**, 2100 (2012).

4. Z. Sun, L. Liu, D. Z. Jia, and W. Pan, Sensors and Actuators B: Chemical **125**, 144 (2007).

5. A. V. Raut, R. S. Barkule, D. R. Shengule, and K. M. Jadhav, Journal of Magnetism and Magnetic Materials **358–359**, 87 (2014).

6. E. R. Kumar, R. Jayaprakash, G. S. Devi, and P. S. P. Reddy, Journal of Magnetism and Magnetic Materials **355**, 87 (2014).

7. H. Pan, L. Zhou, W. Zheng, X. Liu, J. Zhang, and N. Pinna, Int. J. Extrem. Manuf. **5**, 022008 (2023).

8. S. Srivastava, P. Pal, D. K. Sharma, S. Kumar, T. D. Senguttuvan, and B. K. Gupta, ACS Mater. Au **2**, 356 (2022).

9. S. R. Sriram, S. R. Parne, N. Pothukanuri, and D. R. Edla, Journal of Analytical and Applied Pyrolysis **164**, 105527 (2022).

10. R. Vinodkumar, K. J. Lethy, P. R. Arunkumar, R. R. Krishnan, N. Venugopalan Pillai, V. P. Mahadevan Pillai, and R. Philip, Materials Chemistry and Physics **121**, 406 (2010).

11. R. R. Salunkhe, D. S. Dhawale, U. M. Patil, and C. D. Lokhande, Sensors and Actuators B: Chemical **136**, 39 (2009).

12. S. Sagadevan, K. Pal, Z. Z. Chowdhury, and M. E. Hoque, Mater. Res. Express **4**, 075025 (2017).

13. F. Yakuphanoglu, M. Caglar, Y. Caglar, and S. Ilican, Journal of Alloys and Compounds **506**, 188 (2010).

14. A. V. Moholkar, G. L. Agawane, K.-U. Sim, Y. Kwon, K. Y. Rajpure, and J. H. Kim, Applied Surface Science **257**, 93 (2010).

15. D. Bouokkeze, J. Massoudi, W. Hzez, M. Smari, A. Bougoffa, K. Khirouni, E. Dhahri, and L. Bessais, RSC Adv. **9**, 40940 (2019).

16. J. R. Orives, W. R. Viali, M. Magnani, and M. Nalin, (n.d.).

17. A. Hadded, J. Massoudi, E. Dhahri, K. Khirouni, and B. F. O. Costa, RSC Adv. **10**, 42542 (2020).

18. P. K. Nayak, Materials Chemistry and Physics **112**, 24 (2008).

19. N. M. Deraz and M. M. Hessien, Journal of Alloys and Compounds **475**, 832 (2009).

20. S. M., S. G. T.C., and V. G., Journal of Molecular Liquids **256**, 519 (2018).

21. N. R. Reddy, P. M. Reddy, T. K. Mandal, A. K. Yedluri, and S. W. Joo, Journal of Energy Storage **43**, 103302 (2021).

22. M. Naseri, Journal of Magnetism and Magnetic Materials **392**, 107 (2015).

23. B. S. Surendra, H. N. Sowmya, K. N. Harish, M. Bhaskar, K. T, P. T, N. Basavaraju, S. Reddy, and P. K. Sharanya, Ionics **31**, 6409 (2025).

24. B. S. Surendra, M. M. Swamy, B. R. Vergis, M. Bhaskar, C. D. Shilpa, S. Khasim, K. Y. Chan, and H. C. A. Murthy, Sci Rep **14**, 26460 (2024).

25. J. Chen, J. Zhan, E. Lu, Y. Wan, Z. Jin, and H. Qi, Materials Letters **220**, 66 (2018).

26. S. B. Kokane, S. R. Suryawanshi, R. Sasikala, M. A. More, and S. D. Sartale, Materials Chemistry and Physics **194**, 55 (2017).

27. R. J. Deokate, H. S. Chavan, H. Im, and A. I. Inamdar, Ceramics International **48**, 795 (2022).

28. M. M. El-Masry and M. M. Arman, Sci Rep **15**, 16636 (2025).

29. E. A. Davis and N. F. Mott, Philosophical Magazine **22**, 0903 (1970).

30. F. Miao, Z. Deng, X. Lv, G. Gu, S. Wan, X. Fang, Q. Zhang, and S. Yin, Solid State Communications **150**, 2036 (2010).

31. A. Hidri, L. B. Ammar, M. Nasri, J. Khelifi, and E. K. Hlil, J Supercond Nov Magn **38**, 140 (2025).

32. S. A. Mazen, A. S. Nawara, and N. I. Abu-Elsaad, Ceramics International **47**, 9856 (2021).

33. M. E. Hajlaoui, R. Dhahri, N. Hnainia, A. Benchaabane, E. Dhahri, and K. Khirouni, Materials Science and Engineering: B **262**, 114683 (2020).

34. B. Tataroğlu, Ş. Altındal, and A. Tataroğlu, Microelectronic Engineering **83**, 2021 (2006).

35. M. A. Dar, F. Ahmad, M. Ashraf, and A. U. Rehman, (n.d.).

36. Y. L. Huang, W. B. Fan, Y. H. Hou, K. X. Guo, Y. F. Ouyang, and Z. W. Liu, Journal of Magnetism and Magnetic Materials **429**, 263 (2017).

37. T. Tatarchuk, Nanomaterials **14**, 1640 (2024).

38. M. Seki, H. Tabata, H. Ohta, K. Inaba, and S. Kobayashi, Applied Physics Letters **99**, 242504 (2011).

39. M. Benhaliliba and C. E. Benouis, Semiconductors **58**, 750 (2024).

40. A. Kumar, S. Mukherjee, S. Sahare, and R. K. Choubey, Materials Science in Semiconductor Processing **122**, 105471 (2021).

41. M. S. Al-Ghamdi, N. A. Alanazi, and I. Karomi, (2024).

42. S. Douafer, H. Lahmar, M. Benamira, R. Laouici, A. Sahmi, and M. Trari, Reac Kinet Mech Cat **138**, 1845 (2025).